

Depth-of-field extension and 3D reconstruction in digital holographic microscopy

Isabelle Bergoënd^a, Tristan Colomb^b, Nicolas Pavillon^a, Yves Emery^b and Christian Depeursinge^a

^aAdvanced Photonics Laboratory, Ecole Polytechnique Fédérale de Lausanne (EPFL),
CH-1015 Lausanne, Switzerland;

^bLyncée Tec SA, PSE-A, CH-1015 Lausanne, Switzerland

ABSTRACT

The limited depth-of-field is a main drawback of microscopy that prevents from observing, for example, thick semi-transparent objects with all their features in focus. Several algorithms have been developed during the past years to fuse images having various planes of focus and thus obtain a completely focused image with virtually extended depth-of-field. We present a comparison of several of these methods in the particular field of digital holographic microscopy, taking advantage of some of the main properties of holography.

We especially study the extended depth-of-field for phase images reconstructed from the hologram of a biological specimen. A criterion of spatial measurement on the object is considered, completed with a visual criterion. The step of distance taken into account to build the stack of images is less than the instrument depth-of-field.

Then, preserving the distance of focus associated with each pixel of the image, a three-dimensional representation is presented after automatic detection of the object. The limits of such a method of extraction of 3D information are discussed.

Keywords: Digital holographic microscopy, depth-of-field extension, 3D reconstruction

1. INTRODUCTION

Optical devices having a large numerical aperture, like microscopes, are limited by a small depth-of-field sometimes not sufficient to observe all the features of a thick object in one view. Several algorithms have been developed during the past years to fusion images having various planes of focus and thus obtain a completely sharp image. Nevertheless, in classic microscopy only a limited step can be imposed on the mechanical system to change the focus plane. Digital holographic microscopy overcomes this disadvantage by permitting an image reconstruction in any plane parallel to the hologram plane. The reconstruction plane can therefore be moved with an arbitrary step. Moreover, digital holography gives access not only to the image intensity but also to the phase carrying information on the variations of refraction index, which may be very useful to observe internal structures into transparent biological objects.

Most of the extended depth-of-field algorithms used in classic microscopy aim at merging several images of the same object, each of them being partially focalized, depending on the distance of each inner object. To find the focused regions, one of the first idea consisted in looking for the extrema of amplitude.¹ This method gives satisfying results only when the image has a good contrast everywhere. Better results are obtained when calculating the energy contained in each region of the images after high-pass filtering.² Many methods, like gradient or Tenengrad's method, use the pixels in the neighborhood of the current one and define a criterion of sharpness^{1,3,4,5,6}. Another suggestion is the reconstruction of a focused image using, for each pixel, a combination of the corresponding pixels taken from each of the partially focused images.⁷

Further author information: (Send correspondence to I. Bergoënd)

I. Bergoënd: E-mail: isabelle.bergoend@epfl.ch

C. Depeursinge: E-mail: christian.depeursinge@epfl.ch

The previous algorithms have generally not been studied in the particular case of digital holography. Ferraro *et al.* studied focalization and 3D reconstruction especially in holographic microscopy using the distance information carried by the phase image.⁸ This technique is used in the case of surface imaging of reflective objects or for transmitting objects of uniform index of refraction, like microlenses. Wavelet methods, due to their ability to compute localized spatial frequencies, are sometimes used to reconstruct focused images.⁹ Fresnelets were especially developed for holographic purposes.¹⁰

In this paper, we present a comparison of various existing algorithms for depth-of-field extension that we apply to digital holographic microscopy. Then, using the inherent ability of these algorithms to retain the distance of each in-focus region, we perform a 3D reconstruction of the objects of interest, with images obtained from biological phase objects.

2. CONSTRUCTION OF THE FOCUSED IMAGE

2.1 Construction of a stack of images

Digital holographic microscopy benefits from several advantages compared to classic microscopy:

- all the images to be merged can be obtained from a single hologram, recorded experimentally. A satisfying reconstruction can therefore be performed even in the case of time evolution of the object, and misalignment from one image to the other is avoided.
- the step of reconstruction distance can be made as small as needed to build the focused image and can be adjusted precisely, because no mechanical movement is involved. This is well suited to depth-of-field extension.
- the whole complex field is computed, which permits in particular to observe transparent objects only characterized by their variations of refraction index, using the phase images.

In our case, from a hologram typically recorded in transmission through a microscope objective using a Mach-Zehnder interferometer, the virtual image is selected in the Fourier plane and a numerical parametric lens is computed in order to correct the tilt aberration, the phase offset and the wavefront curvature¹¹¹². The mean focus distance, roughly corresponding to the center of the thick specimen, is found visually or using an autofocus algorithm.¹³ A range of distances to be investigated and a longitudinal step are then chosen to generate the stack of images. Two conditions have to be respected. Firstly, the range of reconstruction distances covers the entire object thickness, thus every part can be focused inside the stack. Secondly, the step is less than the microscope depth-of-field so that each sub-structure is sufficiently sampled in the longitudinal direction. As any reconstruction distance can be computed in digital holography, these conditions can always be fulfilled. From this stack of images, we compute several algorithms for depth-of-field extension and compare the final focused images. As our second purpose is to perform a 3D reconstruction, we mostly make use of algorithms that retain one slice of the stack (one distance of focus) for each pixel, instead of a combination of several stacks. The chosen methods will be described in the next section.

2.2 Description of the tested focusing algorithms

The chosen methods are: (A) sum-modified Laplacian,⁴ (B) variance or standard deviation,⁵ (C) local variance weighted averaging,⁶ (D) Tenengrad,⁵ (E) Pieper and Korpel's differential operator,¹ (F) gradient³⁵ and (G) Eltoukhy's combination of pixels.⁷ We also use (H) the software developed by B. Forster *et al.*⁹ to compare the previous algorithms with a wavelets-based method, here complex Daubechies wavelets. For every method using the pixel's neighbourhood (A-D, G and H), we compute the criterion pixel by pixel in a $N \times N$ region ($3 \leq N \leq 25$) and shift the region with overlapping to compute the next pixel, contiguous to the previous one, as depicted in Fig. 1. To save time, it is possible not to overlap the regions.

Let $f_k(x, y)$ be value (intensity or phase) at the pixel (x, y) of the k^{th} image in the stack. The following algorithms will be tested in each small region of size $N \times N$ in the images. $i \leq N$ and $j \leq N$ are indices defined inside the small region. For each of the following methods M , $F_{M,k}$ is the function whose values are

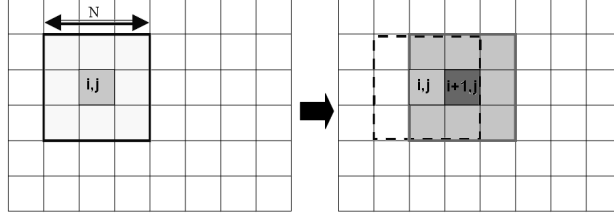


Figure 1. Implementation of the algorithms on contiguous pixels: the output value of the focusing algorithm is computed in a $N \times N$ region around a pixel (i,j) . The value for the pixel $(i+1,j)$ is computed inside a region of the same size overlapping the previous one. Here $N = 3$.

compared to find the slice in which each region is in focus. At the point (x, y) , the pixel from slice k is retained if $F_{M,k}(x, y) = \max_p(F_{M,p})$.

The Laplacian operator is modified with absolute values to prevent opposite terms from cancelling each other:

$$\nabla^2 f_k(x, y) = |2f_k(x, y) - f_k(x - 1, y) - f_k(x + 1, y)| + |2f_k(x, y) - f_k(x, y - 1) - f_k(x, y + 1)| \quad (1)$$

The focused image intensity according to SML (algorithm A) is then:

$$F_{A,k} = \sum_{i=x-N}^{x+N} \sum_{j=y-N}^{y+N} \nabla^2 f_k(i, j) \quad (2)$$

for $f_k(i, j) \geq T$ where T is a facultative threshold.

Algorithm B uses standard deviation. The computed image is:

$$F_{B,k} = \sqrt{\frac{1}{N^2 - 1} \sum_{i=1}^N \sum_{j=1}^N (f_k(i, j) - m)^2} \quad (3)$$

where $m = \frac{1}{N^2} \sum_{i=1}^N \sum_{j=1}^N f_k(i, j)$ is the mean value of f_k in the small region.

Algorithm C consists in computing the average among the values of f_k in all the images of the stack, for each pixel. The values being used for the average calculation are weighted with the local spatial variance around the current pixel. Consequently, in the final image, each pixel is a combination of the corresponding pixels of the stack.

$$F_{C,k}(x, y) = \frac{1}{V} \sum_{k=1}^K \text{var}_N(f_k(x, y)) \cdot f_k(x, y) \quad (4)$$

Here $\text{var}_N(f_k(x, y))$ is the variance computed in a region of size $N \times N$ of the k^{th} image, around the pixel (x, y) . $V = \sum_{k=1}^K \text{var}_N(f_k(x, y))$ is a normalization factor. K is the number of images in the stack.

Tenengrad's method (algorithm D) uses the Sobel high pass filter of size 3×3 with possibly a threshold: $\nabla S(i, j) \geq T'$.

$$F_{D,k} = \sum_{i=2}^{N-1} \sum_{j=2}^{N-1} (\nabla S(i, j))^2 \quad (5)$$

$$\nabla S(i, j) = \sqrt{\nabla S_x(i, j)^2 + \nabla S_y(i, j)^2} \quad (6)$$

$\nabla S_x(i, j)$ and $\nabla S_y(i, j)$ are the respectively horizontal and vertical Sobel filters: $\nabla S_x(i, j) = \begin{pmatrix} 1 & 0 & -1 \\ 2 & 0 & -2 \\ 1 & 0 & -1 \end{pmatrix}$

and $\nabla S_y(i, j) = \begin{pmatrix} 1 & 2 & 1 \\ 0 & 0 & 0 \\ -1 & -2 & -1 \end{pmatrix}$.

Pieper and Korpel's method (algorithm E) lies on a non-directional differential operator always computed in a 3×3 region:

$$F_{E,k}(x, y) = |f_k(x-1, y+1) - f_k(x+1, y-1)| + |f_k(x+1, y+1) - f_k(x-1, y-1)| \\ + |f_k(x, y+1) - f_k(x, y-1)| + |f_k(x-1, y) - f_k(x+1, y)| \quad (7)$$

Algorithm F uses the energy of the gradient image:

$$F_{F,k}(x, y) = \sum_{i=1}^N \sum_{j=1}^N (f_x^2 + f_y^2) \quad (8)$$

with: $f_x = f_k(x, y) - f_k(x-1, y)$ and $f_y = f_k(x, y) - f_k(x, y-1)$. Another definition uses absolute values instead of squared values.

Eltoukhy's method (algorithm G) performs, for each pixel, a combination of the corresponding pixels in the stack. The first step consists in computing the gradient (modified definition involving absolute values) for each pixel of each image. The gradient of image k at pixel (x, y) is written $G_k(x, y)$. In the second step, a so-called majority filter, in which most focused pixels are more weighted, is applied to the stack of images.⁷ We define:

$$\tilde{M}(x, y) = \sum_{i=-N/2}^{N/2} \sum_{j=-N/2}^{N/2} G_k(x+i, y+j) - G_{k+1}(x+i, y+j) \quad (9)$$

$\tilde{M}(x, y) > 0$ means that the pixel (x, y) should be chosen in image k instead of image $k+1$. For more efficiency, a non-linear majority filter is defined as:

$$\hat{M}(x, y) = \frac{1}{1 + e^{-\beta \tilde{M}(x, y)}} \quad (10)$$

The final image is:

$$F_{G,k}(x, y) = \hat{M}(x, y) \cdot f_k(x, y) + (1 - \hat{M}(x, y)) \cdot f_{k+1}(x, y) \quad (11)$$

For more than two images, the following iterative adaptation is proposed:

$$F_{G,k+1}(x, y) = \hat{M}(x, y) \cdot F_{G,k}(x, y) + (1 - \hat{M}(x, y)) \cdot f_{k+2}(x, y) \quad (12)$$

These algorithms will also be compared to Forster's method⁹ which consists in retaining the slice with the highest absolute value of the coefficients from a complex Daubechies wavelet decomposition. A denoising step is also applied.

3. DEPTH-OF-FOCUS EXTENSION

3.1 Results for the tested algorithms

The main existing comparisons of extended depth-of-field algorithms use a set of images artificially generated from which one image is the reference focused image and the others are partially blurred, so that an error between the reference image and the reconstructed one can be calculated. In the case of biological microscopic objects, we only own images obtained with microscopes of limited depth-of-focus. Therefore, in the absence of a reference image, it is not easy to find a criterion of quality for the focalization. We choose two criteria. The first one involves the measurement of the width of some elements in their plane of focus, where they have the smallest size. This measurement is then compared with the corresponding one in the final image and a measurement error is computed. The second criterion is a visual one, where we attribute a mark to the final images according to the visibility of the expected features located in different planes in a biological specimen, also taking into account the map of the numbers of the slices in which each pixel was taken. The same study was performed for $N = 3$, $N = 15$ and $N = 25$ for the concerned algorithms. The best algorithms according to our study, in each case, are presented in table 1.

Table 1. Best-marked algorithms for the size measurement, visual appreciation and execution time criteria. Last row: all the tested methods are taken into account. Other rows: only those using varying N are considered.

	Object measurement	Visual criterion	Execution time
Best algo. among A-D and F-G, $N = 3$	Weighted mean (C)	Tenengrad (D)	Gradient (F)
Best algo. among A-D and F-G, $N = 15$	Tenengrad (D)	St. deviation (B)	Gradient (F)
Best algo. among A-D and F-G, $N = 25$	St. deviation (B)	St. deviation (B)	Gradient (F)
Best overall algorithm	St. dev. (B) $N = 25$	Wavelets (H)	Pieper-Korpel (E)

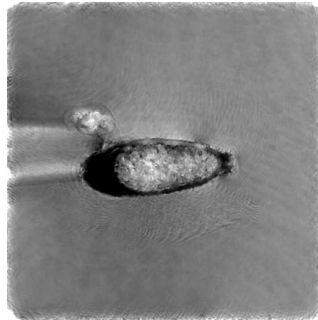


Figure 2. One partially focused image (unwrapped phase) of the stack. The object is a testate amoeba.

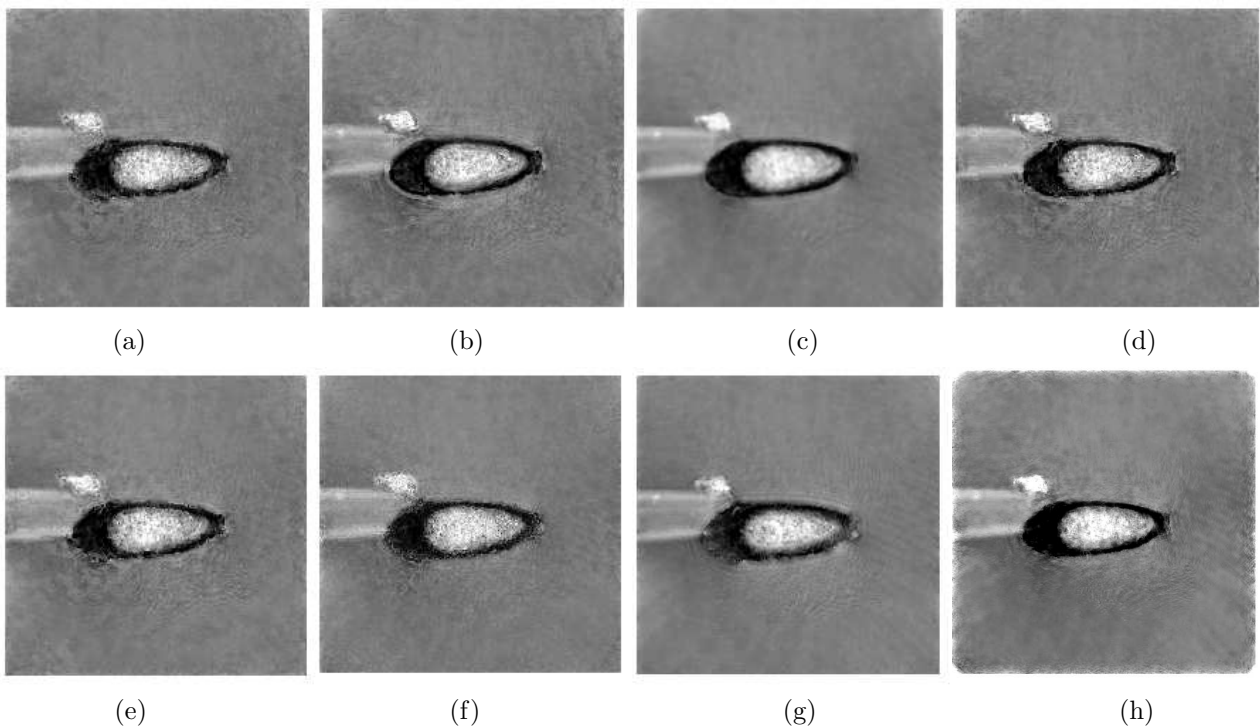


Figure 3. Focused phase images of an amoeba. a: Sum of modified Laplacian. b: Standard deviation. c: Local variance weighted averaging. d: Tenengrad. e: Pieper-Korpel. f: Gradient. g: Eltoukhy. h: Daubechies wavelets with high quality and medium level filtering. $N = 15$, excepted for e and h.

Fig. 2 shows one partially focused image of the biological object used for the tests. As the object is a transparent testate amoeba (*Hyalosphenia papilio*) containing features of varying refractive index, the phase images were used, after 2D unwrapping. A set of images, showing the results of the tested algorithms, is given in Fig. 3. We note that the result must be considered as an image and is no longer a quantitative phase map.

The wavelet method (H) and the standard deviation method (B) both give good visual results for the amoeba and both reach a measurement error less than 10%. We consider them as the best methods of depth-of-field extension for holographic microscopy, whereas execution time for standard deviation is among the longest ones. Algorithm B is suspected to reveal non-existing features when N is small, but this problem disappears for $N \geq 15$. Most of the algorithms well retrieve the object edges but perhaps not so well the internal structures having a weaker contrast. Further examination of the retrieved depth maps reveals that algorithms B ($N \geq 15$), D ($N = 15$) and H best reconstruct the expected edges with satisfying retrieval of the inner structures. Algorithm C acts like a low-pass filter (Fig. 3 c), which may disturb the image understanding in some cases. Pieper and Korpel’s operator method is very fast and gives a visually satisfying focused image, but with high-frequency noise in the map of the retrieved distances. Finally, Eltouky’s method seems to be dependent on the order of the images in the stack and does not retrieve precisely the distances.

3.2 Reduction of the diffraction patterns

As digital holography deals with coherent light, diffraction patterns occur along objects of the order of the wavelength. They may also be the result of a convolution between the limited aperture of the microscope and the objects. This patterns are often considered by the previous algorithms as focused features because of the high spatial frequencies they contain. Two examples of this issue can be seen on Fig. 4. Image a) shows the focused amplitude image of two small balls obtained with algorithm B ($N = 15$). Diffraction rings are clearly visible around the small ball. Image b) is a phase detail of the amoeba seen in Fig. 3, also obtained with algorithm B ($N = 15$). On the bottom left of the object one can see at least two edges instead of one, a black one and a bright one. This may cause a wrong detection of some objects’ edges and a wrong estimation of their sizes or shapes.

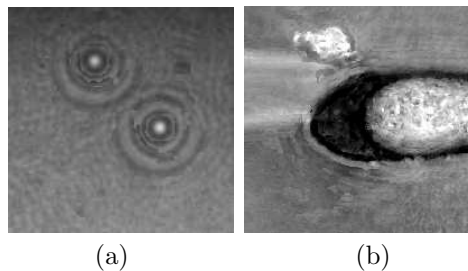


Figure 4. a: Focused amplitude image of two small balls of $1 \mu\text{m}$, showing diffraction rings. b: Focused phase image detail of an amoeba, showing a double edge due to diffraction at bottom left.

Consequently, it is important to reduce these diffraction patterns. If, for a given point of observation located in the neighborhood of a diffracting object, the distance necessary to get a significant displacement of the fringes is smaller than the depth-of-field, the diffraction pattern may be deleted by averaging two consecutive images having an appropriate gap of distance without degrading the reconstruction of the focused image.

We have studied the removal of the rings visible in phase images that are produced by small balls fixed at various depths into a gel. At this stage we must emphasize some specificity of the hologram reconstruction technique. As our phase patterns are considered as images, not as phase maps, the increasing term of phase that normally occurs along the wave propagation must be cancelled, otherwise the images of the stack would not be comparable. In particular, the background would not remain at the same level. Furthermore, attention has to be paid to the procedure, involving a numerical parametric lens, that we use to compensate for the tilt aberration due to the off-axis geometry, the phase delay between the object and the reference waves and the wavefront curvature coming from the microscope optics.¹¹ To ensure the processing parameters of these procedure are the

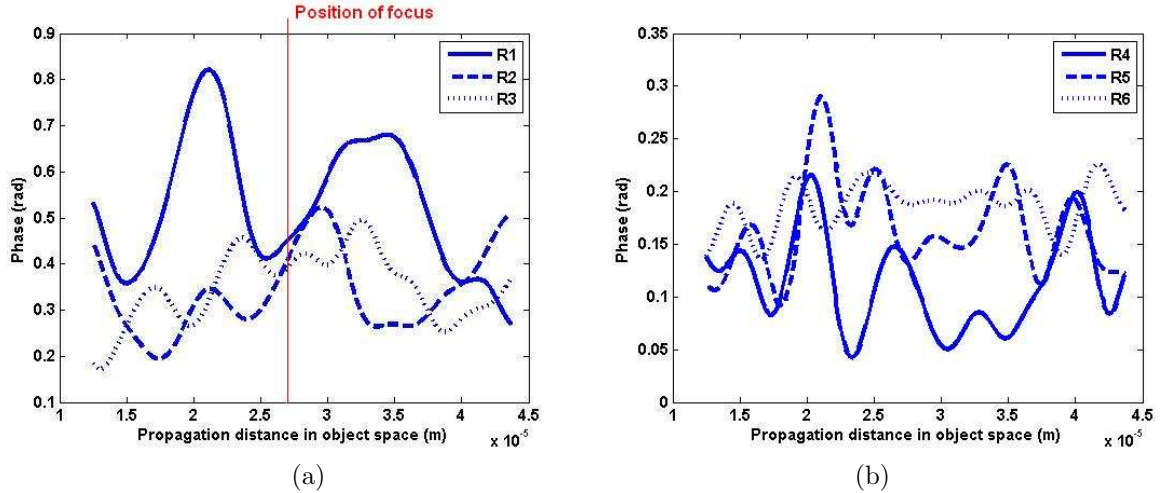


Figure 5. Variations of phase in the diffraction rings with increasing distance of reconstruction, not including the increasing phase term due to propagation. a: Near focus small ball. Radial distances from the center of the diffraction pattern: R1=0.8 μm , R2=2.26 μm , R3=2.74 μm . b: Out-of-focus small ball. R4=10 μm , R5=18.9 μm , R6=23.2 μm .

same in the whole stack, no correction is applied after the propagation stage and the correcting phase mask in the hologram plane is the same for all images.

Fig. 5 shows phases measured at several points in our reconstructed holograms when the distance of reconstruction varies. Following the considerations above, the plotted values must not be considered as representative of the physical evolution of the phase during propagation, but as the variation of gray level in our images. On plot a) the measurements are performed in the neighborhood of a small ball around its focus plane. When the measurement point departs from the object, the phase variation is faster. The phases presented on plot b) concern diffraction rings for a small ball located out of the range of observation. The mean longitudinal distance between two maxima of phase for the farther small ball is less than that of the small ball near focus. For the out-of-focus small ball, the distance necessary to change a minimum into a maximum of phase value is of the same order than the depth-of-field, estimated around 3 microns, thus we expect that the corresponding rings can be partially removed by averaging the consecutive images two by two while preserving a step of reconstruction distance less than the depth-of-field. The advantage of removing such rings is the improvement of the background quality of focused images by decreasing the impact of out-of-focus objects. Nevertheless, around the small balls nearly in focus, the rings will not be entirely cancelled by averaging of the consecutive images.

The result of focused image reconstruction with this averaging is given in Fig. 6 c) and d). One can see that rings and noise have been efficiently removed from the background, compared to the focused image b) without averaging and to the partially focused image a). On image c) the small balls are still well focused but, as expected, for each ball at least one of the main rings has not been cancelled by averaging. The reason why the remaining ring is the one with the smallest amplitude of variation (R6 on Fig. 5 b) has not been explained. Image d) shows the effect of a step of distance between the images of the stack larger than the depth-of-field: the focused features are generally not retrieved.

4. EXTRACTION OF 3D INFORMATION

4.1 Results on the 3D reconstruction

The algorithm chosen for this part of the study must give as an output a single value for the distance of focus for each pixel (or a single slice number in the stack). We choose to use the standard deviation criterion with $N = 15$, which is a good compromise between efficiency and computation time. As a given focused image often consists of an object superposed to a background, the region of interest has to be selected before performing the 3D reconstruction. This is done by preserving only the pixels that exhibit a standard deviation greater

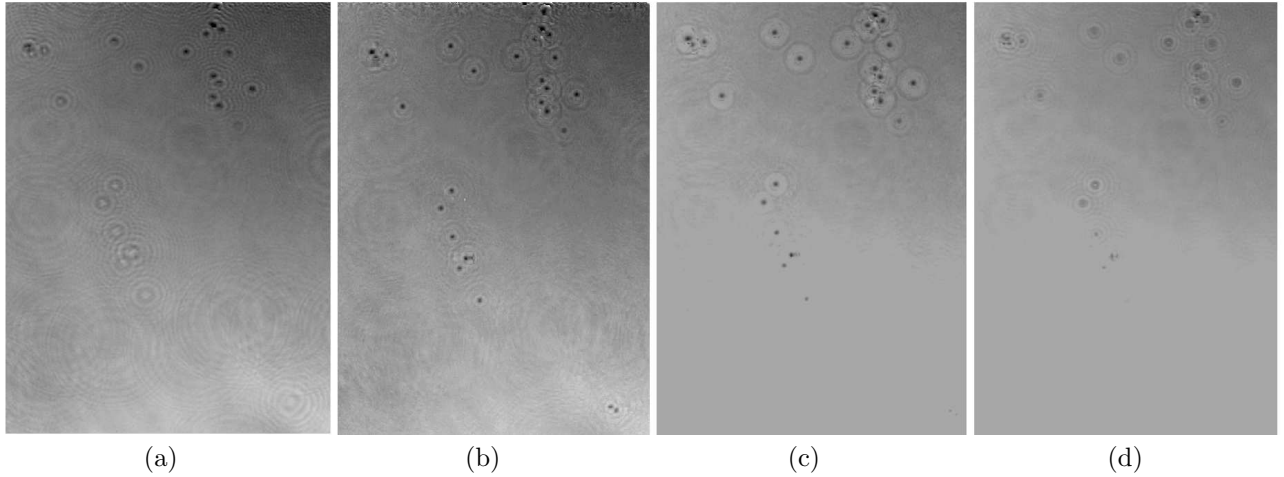


Figure 6. Result of rings cancelling in phase images. (a) One image of the stack, with limited depth-of-field. (b) Image with extended depth-of-focus, algorithm B with $N = 15$. (c) Image with extended depth-of-focus and averaging of the consecutive images two by two, longitudinal step of 78 nm. (d) Image with extended depth-of-focus and averaging of the consecutive images two by two, longitudinal step of 10 μm , too large compared to the depth-of-field.

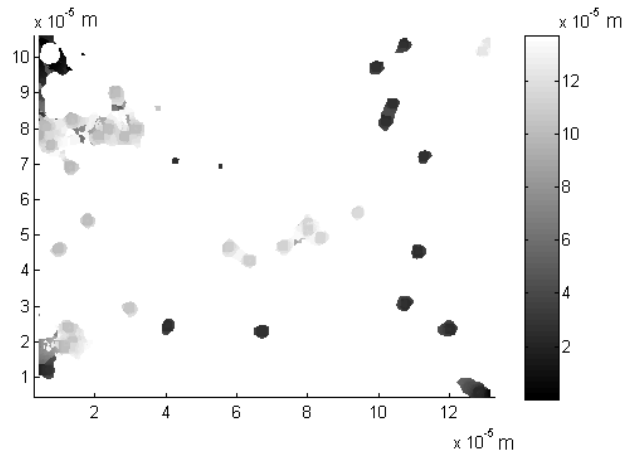


Figure 7. 3D representation of small balls in a gel. Focusing algorithm used: standard deviation with $N = 15$. Longitudinal distances are relative to the position of the stack.

than a threshold. The threshold can be adjusted manually while the regions above the current threshold are automatically displayed by our software. A compromise has to be found between the presence of some noise around the objects and the possible cancellation of the least-contrasted objects of interest. As edges often lead to higher values of standard deviation than inner parts of objects, after a spatial consistency check, dilatation and erosion are applied to close the contours. The groups of pixels included into a selected region are taken into the selection to ensure that the regions of interest are convex. Finally, the map composed of slices numbers computed by the variance algorithm is converted into a distance map calculated from the reconstruction distances of the hologram. It is then possible to display a 3D view of the object. Figure 7 shows the results obtained from the hologram of several small balls into a gel. The distances are well rendered, whereas some artifacts appear between the closest balls that are nearly in contact.

4.2 Discussion on the 3D reconstruction

It has to be mentioned that exploitation of three-dimensional information in digital holography is still, to a large extent, an open issue. Despite the number of advantages of digital holography in metrology and imaging, the extraction and exploitation of its inherent 3D information has not been widely studied yet. We have proposed here to adapt a simple method, already used for depth-of-field extension in classic microscopy, to obtain a 3D reconstruction from digital holographic microscopic data. Nevertheless, due to the properties of digital holographic microscopy and in particular the arbitrary distance of reconstruction, 3D information extraction from this technique is more pertinent than in classic microscopy.

As the main property used in the technique is the limited depth-of-field, the longitudinal resolution of the reconstruction mainly depends on it. Each focusing algorithm indeed fails in being more precise than a fraction of the depth-of-field. One consequence of it is that a good optimization of the algorithm consists in the choice of the step of distance in the stack around one half the depth-of-field. If the technique of averaging of the consecutive images two by two is planned to be used, the step has to be divided by 2.

When using this technique of averaging for the suppression of diffraction patterns, the principal goal is to enhance the focused image. However, it tends to modify the local value of focusing algorithms, which leads to a bad detection of some of the objects of interest when the threshold is applied. Thus, some tests must be done on each set of images to decide whether averaging is interesting for 3D reconstruction.

5. CONCLUSION

We have made use of the ability of the holograms to be reconstructed in any plane with arbitrary step of distance to build extended depth-of-field images. Several focusing algorithms developed for classic microscopy have been applied and have been found to be usable in digital holographic microscopy. The two algorithms that best retrieve an entirely focused image, on human observation and measurement criteria, are the wavelet method and the standard deviation algorithm used in subregions of sufficient size. The fastest is Pieper and Korpel's algorithm but it exhibits some noise. A technique of averaging of the consecutive images of the stack two by two has been tested to decrease the effect of diffraction patterns. Its efficiency depends on the evolution of these patterns in relation to the depth-of-field. Finally, using the maps containing the slice numbers retained in the focusing process, a 3D reconstruction of phase images has been shown. As the phase maps are considered as gray-level images where sharp edges are detected, this 3D reconstruction is pertinent even in the presence of phase objects, when optical path lengths alone don't characterize distances but variations of the refractive index.

ACKNOWLEDGMENTS

This work is a part of the project "Real 3D" funded by the European Community's Seventh Framework, programme FP7/2007-2013 under grant agreement n°216105.

REFERENCES

- [1] Pieper, R. and Korpel, A., "Image processing for extended depth of field," *Appl. Opt.* **22**, 1449–1453 (1983).
- [2] Wu, H., Barba, J., and Gil, J., "A focusing algorithm for high magnification cell imaging," *Journal of Microscopy* **184**, 133–142 (1996).
- [3] Wall, R., Sobin, S., Karspeck, M., and Lindal, R., "Computer-derived image compositing," *J. Appl. Physiol.* **51**, 84–89 (1981).
- [4] Nayar, S. and Nakagawa, Y., "Shape from focus," *IEEE Trans. Pattern Analysis and Machine Intelligence* **16**, 824–831 (1994).
- [5] Huang, W. and Jing, Z., "Evaluation of focus measures in multi-focus image fusion," *Pattern Recognition Letters* **28**, 493–500 (2007).
- [6] Sugimoto, S., "Digital composition of images with increased depth of focus considering depth information," *Appl. Opt.* **24**, 2076–2080 (1985).
- [7] Eltoukhy, H. and Kavusi, S., "A computationally efficient algorithm for multi-focus image reconstruction," *Proc. of SPIE Electronic Imaging*, 332–341 (2003).

- [8] Ferraro, P., Grilli, S., Alfieri, D., Nicola, S. D., Finizio, A., Pierattini, G., Javidi, B., Coppola, G., and Striano, V., "Extended focused image in microscopy by digital holography," *Optics Express* **13**, 6738–6749 (2005).
- [9] Forster, B., de Ville, D. V., Berent, J., Sage, D., and Unser, M., "Complex wavelets for extended depth-of-field: a new method for the fusion of multichannel microscopy images," *Microscopy Research and technique* **65**, 33–42 (2004).
- [10] Liebling, M., Blu, T., and Unser, M., "Fresnelets: new multiresolution wavelet bases for digital holography," *IEEE Trans. image processing* **12**, 29–43 (2003).
- [11] Colomb, T., CuChe, E., Charrière, F., Kühn, J., Aspert, N., Montfort, F., Marquet, P., and Depeursinge, C., "Automatic procedure for aberration compensation in digital holographic microscopy and applications to specimen shape compensation," *Applied Optics* **45**, 851–863 (2006).
- [12] Colomb, T., Montfort, F., Kühn, J., Aspert, N., CuChe, E., Marian, A., Charrière, F., Bourquin, S., Marquet, P., and Depeursinge, C., "Numerical parametric lens for shifting, magnification and complete aberration compensation in digital holographic microscopy," *J. Opt. Soc. Am. A* **23**, 3177–3190 (2006).
- [13] Langehanenberg, P., Kemper, B., Dirksen, D., and von Bally, G., "Autofocusing in digital holographic phase contrast microscopy on pure phase objects for live cell imaging," *Appl. Opt.* **47**, 176–182 (2008).